Title
Seismic response to fluid injection and production in two Salton Trough geothermal fields, southern California

Author
Lajoie, Lia Joyce

Publication Date
2012

UNIVERSITY OF CALIFORNIA

SANTA CRUZ

SEISMIC RESPONSE TO FLUID INJECTION AND PRODUCTION IN TWO SALTON TROUGH GEOTHERMAL FIELDS, SOUTHERN CALIFORNIA

a thesis submitted in partial satisfaction
of the requirements for the degree of

MASTER OF SCIENCE

in

EARTH SCIENCES

by

Lia J. Lajoie

December 2012

The thesis of Lia J. Lajoie
is approved:

Professor Emily E. Brodsky

Professor Thorne Lay

Professor Noah J. Finnegan

Tyrus Miller
Vice Provost and Dean of Graduate Studies

TABLE OF CONTENTS

LIST OF FIGURES

LIST OF TABLES

ABSTRACT

Lia J. Lajoie

SEISMIC RESPONSE TO FLUID INJECTION AND PRODUCTION IN TWO SALTON TROUGH GEOTHERMAL FIELDS, SOUTHERN CALIFORNIA

California hosts both the largest geothermal resource capacity and highest seismicity rate in the nation. With plans to increase geothermal output, and proven earthquake triggering in the vicinity of geothermal power plants worldwide, it is important to determine the local and regional effects of geothermal power production. This study examines the link between fluid injection and seismicity at the Salton Sea and Brawley geothermal fields in southern California by attempting to answer three motivating questions: 1) Does fluid injection at the geothermal field change local seismicity in a measurable way? 2) Are aftershocks triggered at the same rate inside and outside of the field? 3) How do the triggered aftershocks interact with regional fault networks, specifically, could these aftershocks trigger a societally significant event on the southern San Andreas or Imperial faults?

Injection and production data consist of monthly logs from 1980 to 2012 for wells at both Salton Sea geothermal fields (California Department of Conservation, 2012). Seismic data for the same time span comes from the relocated Hauksson, Yang, and Shearer earthquake catalog for southern California (2012), which is augmented by the Southern California Seismic Network earthquake catalog (2012). We employ an epidemic-type aftershock sequence model to predict background seismicity and aftershock rates in the geothermal fields, and use empirical earthquake relationships to measure aftershock productivity. Background seismicity rate closely tracks net production volume at the Salton Sea geothermal field for early and late stages of field development and we find that earthquakes inside the field trigger aftershocks at a higher rate than ordinary earthquakes. Finally, we calculate small but finite probabilities that the aftershocks of events in the geothermal fields will trigger significant earthquakes on the large, regional faults, of order 10^{-5} to 10^{-8} per year.

ACKNOWLEDGEMENTS

I would like to thank my advisor, Emily E. Brodsky for her extensive guidance and patience. I would also like to express gratitude to the Southern California Earthquake Center for funding most of the work done in this thesis. There are many people whose conversations have helped guide and stimulate this work, and countless others who have been invaluable for their assistance and/or friendship.

This thesis is dedicated to:

my grandparents, Ken and Andrea Lajoie
for their love and support

and to John Nall
who lives on in the mountains

CHAPTER 1

-BACKGROUND-

The exploitation of geothermal resources has and will continue to expand as the United States increases its reliance on renewable energy sources. Production of geothermal power is shown to induce seismicity as water is pumped into or out of a reservoir, both altering fluid pressure and creating thermal perturbations that may lead to fracturing of the reservoir rock (McGarr et al., 2002; Phillips et al., 2002; Segall and Fitzgerald, 1998). California, with the largest geothermal potential of any state (California Energy Commission, 2010), is also host to a large, active tectonic margin with a high level of natural seismicity. The purpose of this project is to test whether fluid injection and production within the Salton Sea and Brawley geothermal fields in southern California locally increases the rate of seismicity and may also lead to increased activity on proximal faults such as the San Andreas and Imperial faults (Figure 1.1). To do this, we pose three driving questions:

1. Is geothermal power production causing measurable changes in seismicity rates at the Salton Sea and Brawley geothermal fields?
2. Are aftershocks within the Salton Sea geothermal field triggered at the same rate as those outside of the field?
3. How do triggered events and their aftershocks interact with regional fault networks? More specifically, could activity at the Salton Sea geothermal field trigger a large earthquake on the southern San Andreas fault? Could perturbation of the hydrothermal environment at Brawley trigger a large earthquake on the

Imperial fault?

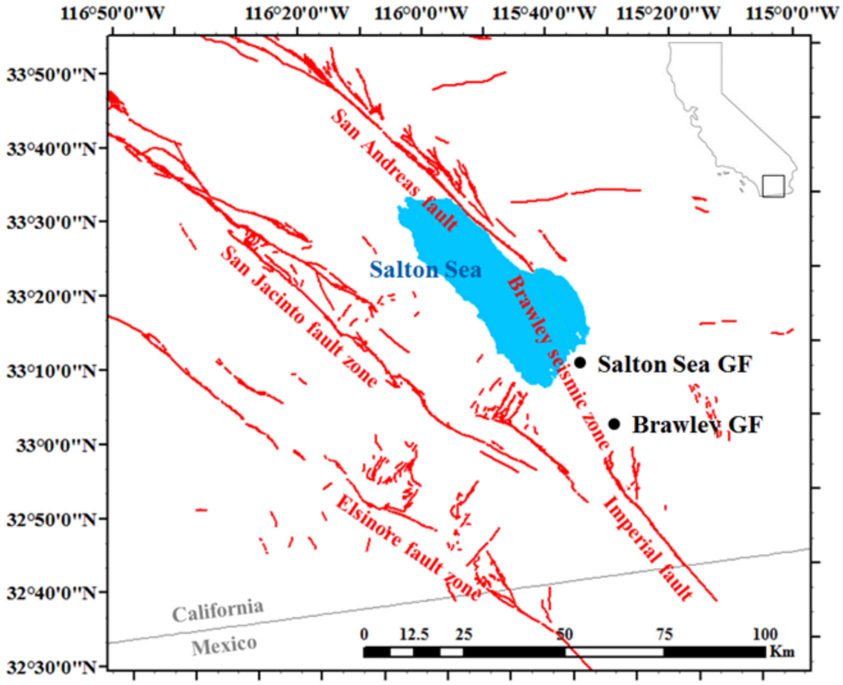

Figure 1.1: Regional map showing faults and the locations of the Salton Sea and Brawley geothermal fields

1.1 GEOLOGIC SETTING

The Salton Sea and Brawley geothermal fields lie in the Salton Trough, near the southern margin of the Salton Sea in southern California (Figure 1.1). The Salton Trough occupies the northern end of the structural basin formed by the intersection of the East Pacific Rise (EPR) with the North American plate, where right lateral motion along the San Andreas fault zone transitions to rifting along the EPR (Muffler and White, 1969; Younker et al., 1982). This transition zone, known as the Brawley Seismic zone, is dominated by en echelon right-stepping, right-lateral faults that create a series of pull-apart basins and thin the Earth's crust between the San Andreas and the Imperial faults (Elders et al., 1972; Muffler and White, 1969; Younker et al., 1982). In the vicinity of the Salton Sea and Brawley geothermal fields, gabbroic basement is overlain by approximately 12 km of primarily Pliocene and Quaternary Colorado River alluvium that includes minor contributions from local sediment sources (Fuis et al., 1984; Muffler and White, 1969; Tewhey, 1977). Below about 4 km depth, the sediments have been extensively metamorphosed to a crystalline greenschist facies due to high heat-flow that is attributed both to thinned lithospheric crust and Quaternary volcanism from leaky transform faults (Fuis et al., 1984; Muffler and White, 1969; Robinson et al., 1976).

The Salton Sea itself is only the latest in a succession of isolated lakes to fill the Salton Trough and was artificially filled in 1905 when a diversion channel taking water from the Colorado River to the Imperial Valley flooded (Van de Kamp, 1973). Its current water level sits about 70 meters below sea level, with a maximum depth of 15 meters (Tompson et al., 2008). Within its closed basin, the Salton Sea receives 90% of its inflow from agricultural runoff, with the remaining 10% divided between natural precipitation, urban use, and groundwater (Redlands Institute, 2002). The water table along the southern shore slopes downward into the lake (Tompson et al., 2008).

1.2 SALTON TROUGH GEOTHERMAL ACTIVITY

The Salton Trough is home to four operating geothermal fields (Salton Sea, Brawley, Heber, and East Mesa) that exploit hot geothermal brine to generate a total of over 600 megawatts of electricity. The Salton Sea geothermal field (SSGF), located on the southern edge of a pull-apart basin, exploits a hot, geothermal brine with a dissolved solids concentration around 250,000 ppm and temperatures in excess of 320° C at 2 km depth (Muffler and White, 1969; Younker et al., 1982). The field includes ten operating geothermal power plants with a net capacity of approximately 330 MW (CalEnergy, 2011). Plants rely on single flash and double flash technologies, whereby pressurized fluid is extracted from depth and some portion flashes to steam as it ascends to the surface. The steam is used to turn turbines and generate electricity, while the remaining brine is either re-injected via separate wells back into the reservoir (single flash), or subjected to a second flashing in a lower pressure chamber before being re-injection (double flash). The difference between extracted and injected water volume, the net production volume, is due to evaporative loss from the cooling process (DiPippo, 2012). Exploratory drilling at the Salton Sea geothermal field began in 1960, and the first plant (Salton Sea I) came online in 1982 (Muffler and White, 1969; CalEnergy, 2011). For the highest producing month in 2012, about $10.5 \cdot 10^9$ kg (approximately 10^7 cubic meters) of geothermal fluid was extracted from the reservoir at depths of about 1 to 2.5 km, and about $8.7 \cdot 10^9$ kg was re-injected to similar depths (we refer to injected volumes rather than masses in the text because it is easier to conceptualize and the constant of proportionality, about 10^3 kg/m^3, is very nearly constant) (California Energy Commission, 2010; California Department of Conservation, 2012).

The Brawley geothermal field (BGF) is a much smaller operation at only 50 MW and with a maximum monthly extraction rate for 2012 of $1.9 \cdot 10^9$ kg (about 10^6 cubic meters) and a corresponding $1.5 \cdot 10^9$ kg of injection (California Department of Conservation, 2012). The mean fluid temperature at Brawley is 253° C (Brook et al., 1978) and is not itself hot enough to use in flash units. The extracted geothermal fluid is instead used to flash a secondary working fluid with a lower boiling point in binary cycle power plants. Much like the flash plants at the SSGF, cooled geothermal fluid is returned to the reservoir via injection wells (DiPippo, 2012).

1.3 OBSERVATIONS

Preliminary studies provide reason to suspect that Salton Sea and Brawley geothermal fields locally increase the number and rate of earthquakes. We qualitatively assess seismic behavior in the geothermal fields by comparing the locations of earthquakes to the locations of wells, and comparing the seismicity rate and energy release to fluid injection at each field. Seismic data is obtained from the Hauksson, Yang, and Shearer (HYS) (2012) relocated earthquake catalog for southern California and is supplemented by data from the Southern California Earthquake Data Center and the Southern California Seismic Network (2012) for those events that have occurred since the HYS catalog was last updated. Injection and production data are available from the California Department of Conservation, Division of Oil, Gas, and Geothermal Resources (2012).

Location plots of earthquakes in the SSGF make it clear that the majority of seismicity clusters around injection wells both at the surface and at depth (Figure 1.2). In plan view, most of the earthquakes plot in diffuse clouds around injection well clusters and extend somewhat to the north, following the local hydrologic gradient (Tompson et al., 2008). Other earthquakes define two sets of lineaments within the field, one striking northeast-southwest and the other north northwest-south southeast, the predominant orientations of regional extensional and strike-slip features, respectively. The majority of seismicity, when seen in cross section, extends in depth from around 2 km down to about 8 km, concentrated in cylinders roughly centered on the groups of injection wells, though there is reason to suspect that the relocated depths are too deep and the majority of seismicity might lie in the shallower alluvium (less than ~ 4km) (Hauksson et al., 2012, Chu and Helmberger, 2012). Most of the events in the BGF, by contrast, cluster in time and locate on roughly NE-SW striking lineaments within the geothermal field (Figure 1.3). Lineaments are consistent with the orientation of regional extensional features, though two large left-lateral strike-slip events ruptured on NE-SW lineaments in the field in August of 2012 (Chu and Helmberger, 2012).

When seismicity rates are compared to injection volume (Figure 1.4), there are both different injection patterns and different seismic responses. At the Salton Sea geothermal field, injection began around the same time that our earthquake catalog begins (HYS catalog completeness at low magnitudes is not trusted before about 1980) and continues today, precluding comparison of pre- and post-injection seismicity rates.

Seismicity rate during initial injection was very low with the exception of one or two swarms until the ramp-up in injection volume between about 1986 and 1990 that was accompanied by high rates of seismicity (Figure 1.4). These years are dominated by two periods of peak seismicity greater than 100 events per month and one greater than 70 events per month. The one notable peak in seismicity rate during the relatively stable injection period between about 1990 and 1996 is concurrent with the magnitude 7.3 Landers earthquake of 1992 that occurred less than 140 km distant.

The background rate during this time was higher than the pre-1986 rate. In 1996, injection volumes again increased, but fluctuated until about 2001, when both the absolute injection volumes and time-scale of oscillations fell. During this time, there were three periods of peak seismicity greater than 50 events per month, as well as a spike in seismic moment in late 1999 that is temporally coincident with the roughly 200 km distant, magnitude 7.1 Hector Mine earthquake. After 2001, injection rate slowly climbed to its maximum monthly rate in 2006, and remained high with higher wavelength oscillations to current time. Background seismicity rate remained high, but the number of distinct high-seismicity events declined to just four in these final years. The largest rate increase in the whole catalog, in late 2005, has previously been studied and classified by Llenos et al. (2009) and Lohman and McGuire (2007) as an earthquake swarm triggered by a local aseismic transient.

We visually isolate three distinct clusters of injection wells and earthquakes at the SSGF (Figure 1.5) and assume that the earthquakes in each are related to the corresponding wells. We plot the same curves that we did for the full field data (Figure 1.6), except with cumulative values and immediately notice that the cluster with the lowest injection volumes also has a lower total number of earthquakes and seismic moment release. The clusters with higher injection volumes have higher numbers of earthquakes and seismic moment released.

At Brawley, in contrast, injection began in 1982 and shut down in 1985, remaining inactive until 2009, when injection began again and continues today (Figure 1.4). This provides a long time window between 1985 and 2009 with good seismic coverage and no injection that can be compared with actively injecting periods. Background seismicity was low during the first injection period of 1982 to 1985 and only contains one notable spike in seismicity. The fluid dormant period from 1985 to 2009 also had low background seismicity and only two seismicity spikes, one in 1999 (more clearly seen in the seismic moment plot) and one in 2008 that has low moment release. The spike in 1999 coincides with the Hector Mine earthquake seen in the Salton Sea geothermal field data; the spike 2008 is peculiar in that it is composed of many small events with no events larger than magnitude three. With the beginning of injection in 2009, background seismicity increased and we observe two spikes in seismicity rate. The first, in December of 2011, occurred during what is by far the highest-volume injection month on record for Brawley, following its largest change in injection volume for consecutive months, and during a month where injection greatly exceeded production. Injection dropped back down to about $1.5 \cdot 10^9$ kg of fluid per month (approximately $1.5 \cdot 10^3$ km^3 per month) and has remained at roughly that volume through August 2012, when the largest seismicity rate in the catalog occurred. The August 2012 swarm included over 600 events in a time span of only 6 days from the 26th to the 31st. It does not behave as a normal aftershock sequence, with the largest event occurring roughly a third of the way through the sequence, and with only about a 0.2 magnitude unit separation between the two largest events.

In the SSGF, seismicity both clusters around injection wells and locates northward, down the local hydrologic gradient, as we would expect earthquakes to do if they were in fact being triggered by migrating fluid pressure pulses. We also notice at both fields that seismicity rate increases as fluid injection rates ramp up and fluctuate, which is consistent with the idea that earthquakes are triggered by transient high-fluid pressure (Shapiro et al., 2010). In the Salton Sea geothermal field, we show that the earthquake and well clusters with higher injection volumes also have higher numbers of associated earthquakes, and suggest a possible scaling relationship between injection volume and number of induced earthquakes. The fact that the earthquakes define lineaments to some degree in both fields also indicates that induced events are interacting with local faults. We conclude that injection at both geothermal fields is locally inducing seismicity.

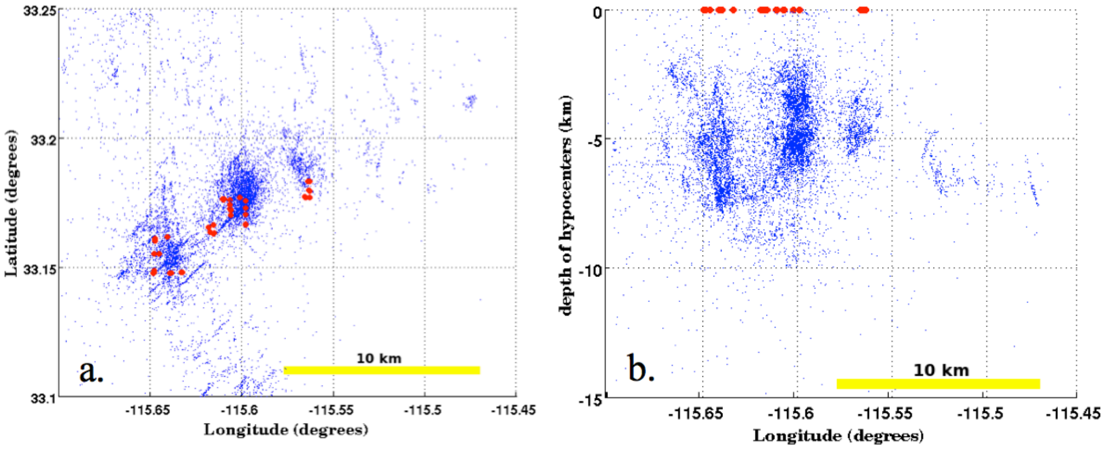

Figure 1.2: Earthquake and well locations for the SSGF. Data includes only HYS catalog data through June 2011. Figure 1.2a: Earthquake epicenters and injection well locations. Figure 1.2b: E-W cross sectional view of earthquake hypocenters showing clustering at depth beneath injection wells.

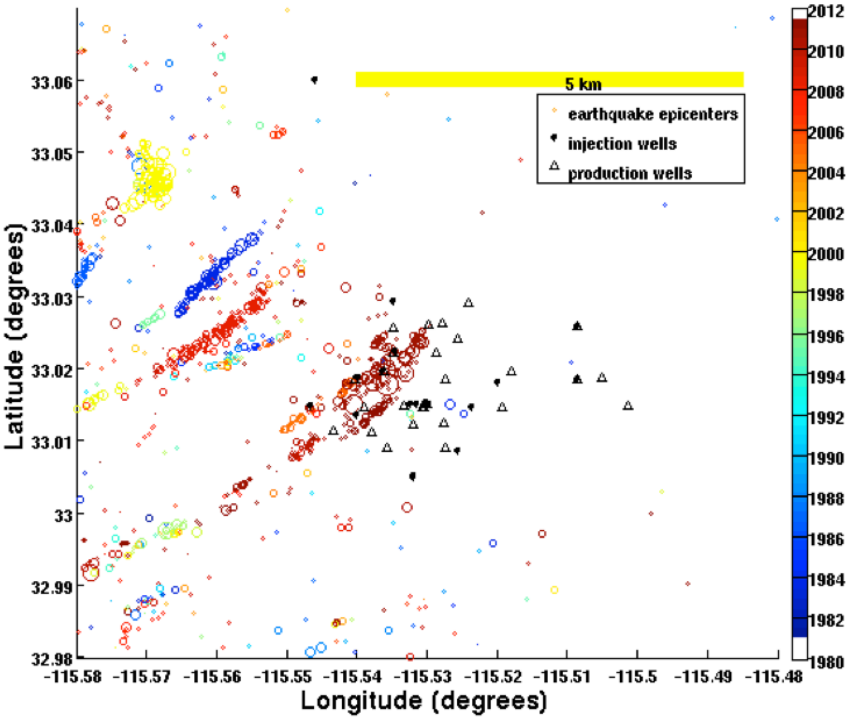

Figure 1.3: Temporal map of earthquake epicenters and well locations at the Brawley geothermal field. Data from the HYS relocated catalog only. Does not include the 2012 swarm.

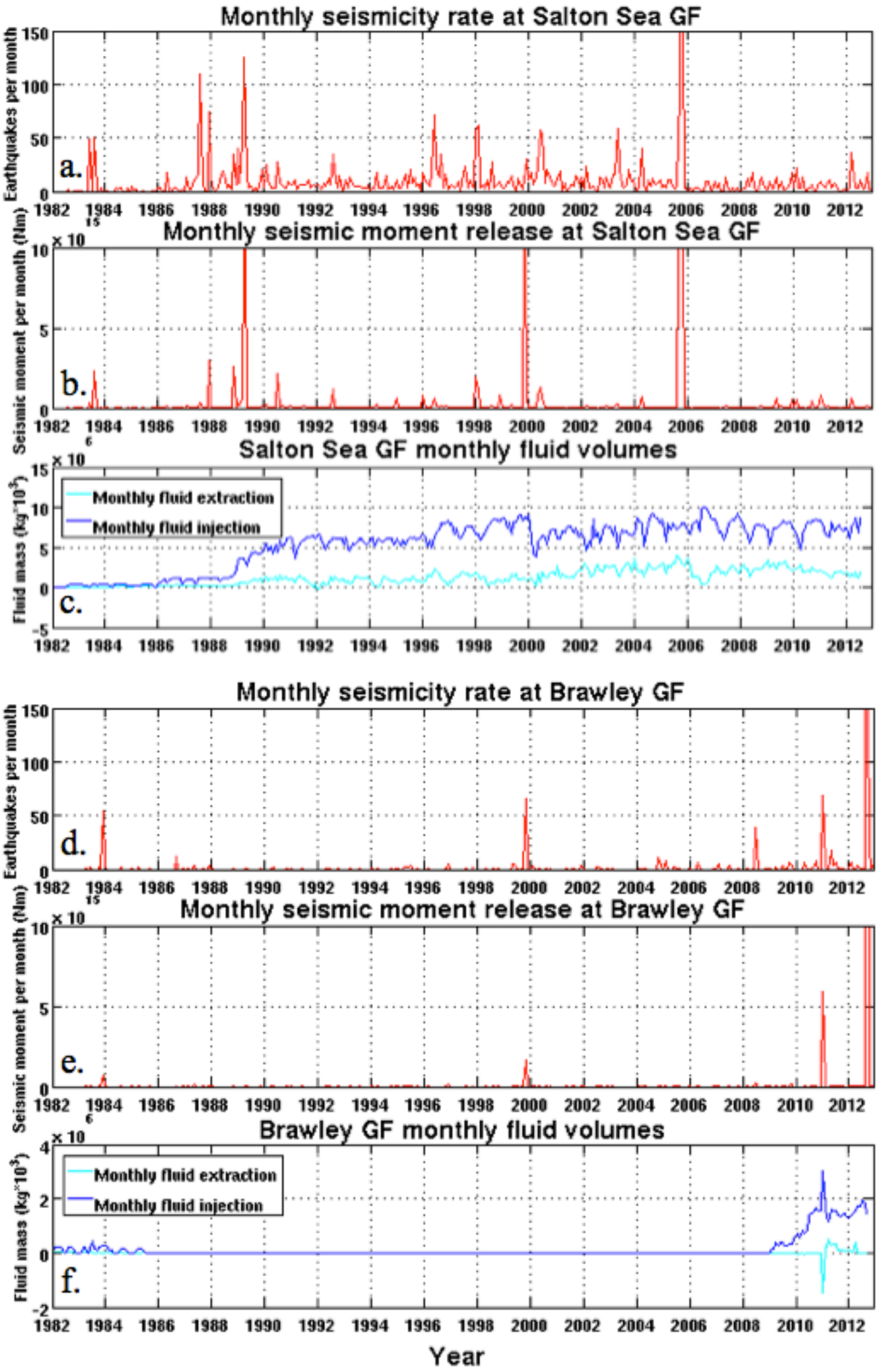

Figure 1.4: Seismicity rate, seismic moment released, and monthly fluid volumes at SSGF (Figure 1.4a-c) and BGF (Figure 1.4d-f). Monthly fluid extraction is the difference between production and injection; negative value indicates injection > production.

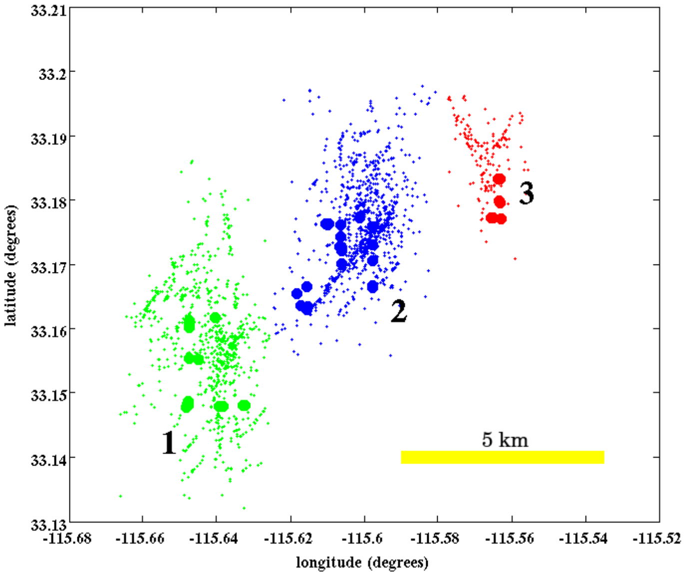

Figure 1.5: Wells and earthquakes seen in Figure 1.2b can be divided into three distinct clusters. It is likely that earthquakes in a given cluster are most influenced by the corresponding wells.

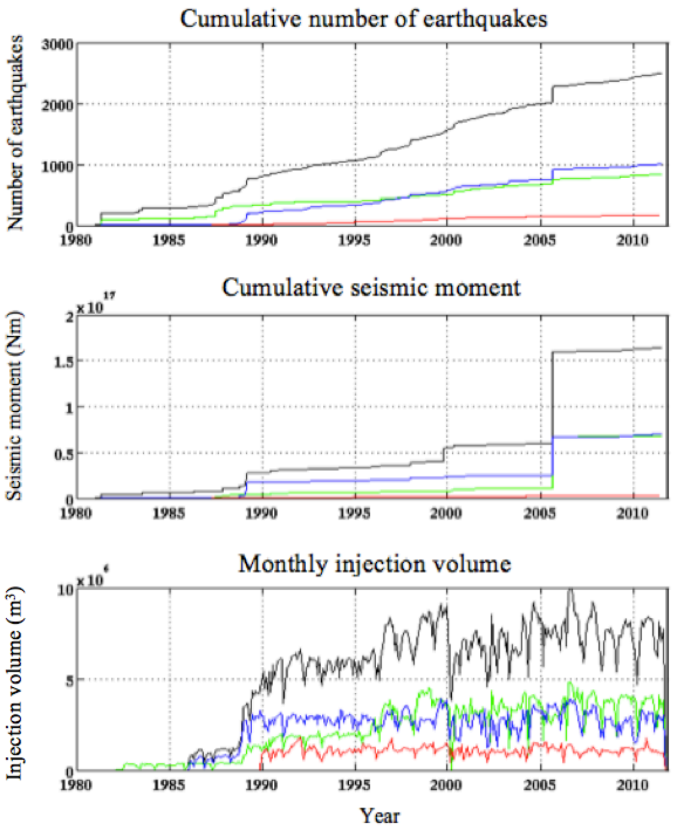

Figure 1.6: Seismic data and fluid injection mass for each of the three clusters in Figure 1.5. Line colors match the swarm colors from Figure 1.5, with black representing data from all earthquakes and wells within the SSGF.

CHAPTER 2

-METHODS: THE ETAS MODEL-

In order to examine both the local response to fluid injection and the regional effects of seismicity induced by fluid injection, we model seismicity using an Epidemic-Type Aftershock Sequence (ETAS) method. The intensity function that describes the seismicity rate at some point in time, t_E, is a combination of a modified Omori's law (Omori, 1894; Ustu, 1961; Utsu et al., 1995) and the Gutenberg-Richter relation (Gutenberg and Richter, 1954) and is given by

$$R_{ETAS}(t_E) = \mu + \sum_{t_E \le t_i} \frac{K_E \cdot 10^{\alpha(M_i - M_c)}}{(t_E - t_i + c)^p} \tag{1}$$

where μ is the background seismicity rate and the term inside the summation describes the component of seismicity due to aftershock sequences. In this formulation, K_E is the aftershock productivity of a mainshock, α describes the efficiency of earthquakes of a given magnitude at generating aftershocks, c and p are Omori's law decay parameters, M_i and t_i are the magnitude and time of the i^{th} event in some catalog, and M_c is the magnitude completeness threshold of that catalog (Ogata, 1992). The expected cumulative number of earthquakes, $\Lambda(T)$, in some time period [S,T] is the time integral of R_{ETAS} over that interval (Ogata, 1988).

In this study, we constrain α to be 1 following the work of Felzer et al. (2004) and Helmstetter et al. (2005) and only solve for the remaining four free parameters in equation 1 (μ, K_E, c, p). For the Salton Sea geothermal field, we calculate $M_c = 1.7$ using Gutenberg Richter (Appendix A) (1954). Optimization is achieved via a maximum (log) likelihood method. The log likelihood function for an inhomogeneous Poisson point-process with history dependent intensity function, $\lambda(t \mid H_t)$, is given by

$$\ln L(\Theta; S, T) = \sum_{i=1}^{N} \ln \lambda_0(t_i \mid H_i) - \int_S^T \lambda_0(t_i \mid H_i)\, dt \tag{2}$$

where θ is a vector of parameters (μ, K_E, c, α, p), N represents the total number of events, and the observation is over a time interval [S,T] (Snyder and Miller, 1991; Ogata, 1992). The combination of parameter values that maximizes this likelihood is considered to be the best fit to the data. In this study, R_{ETAS} represents the conditional intensity and the likelihood function to maximize becomes

$$\ln L(\Theta; S, T) = \sum_{j=1}^{N} \ln\left[\mu + \sum_{i=1}^{j} \frac{K_E \cdot 10^{\alpha(M_i - M_c)}}{(t_j - t_i + c)^p}\right] - \int_S^T \left[\mu + \sum_{t_E \le t_i} \frac{K_E \cdot 10^{\alpha(M_i - M_c)}}{(t_E - t_i + c)^p}\right] dt_E \tag{3}$$

Maximization is performed by finding the minimum of the negative log-likelihood function using a constrained quasi-Newtonian minimizer. Error bars are one standard deviation inferred from the curvature of the likelihood space for each parameter. We first test our inversion code on synthetic (test) catalogs to ensure that correct parameter values are returned. The resulting parameter values for the SSGF are reported in Table 2.1.

Parameters c, K_E, and α can be calculated empirically as a second confirmation that inversions are functioning properly. We first check the value of c, which measures the average amount of time after a given mainshock that aftershocks cannot be detected due to the smaller amplitude seismic waves of aftershocks being effectively “hidden” in the larger amplitude signals of the mainshock. We understand from inversions on synthetic data sets with known parameter values that c tends to be very unstable. Its predicted value seems to influence the value of p returned by our inversions, but has little effect on the values of *K*, *μ*, or *α*. For the Salton Sea geothermal data, we calculate *c* = 0.006 days (Appendix B), which is drastically different than the ETAS predicted value. Knowing the tradeoffs between *c* and *p* in ETAS inversions, we use our calculated value of *c* = 0.006 in all further calculations and set *p* = 1.1 following the work of Hardebeck et al. (2008).

The values for *K* and *α* are independently confirmed in aftershock productivity calculations (Chapter 4.2).

Parameter	*ETAS value*		*Value used in calculations for Chapters 3 and 4*
K	$1.3 \cdot 10^{-2}$	$\pm 1.4 \cdot 10^{-3}$	$1.3 \cdot 10^{-2}$
c	0.30	$\pm 4.0 \cdot 10^{-2}$	0.006
p	1.5	$\pm 5.5 \cdot 10^{-2}$	1.1
μ	0.11	$\pm 4.6 \cdot 10^{-3}$	0.11
α	*1		1

Table 2.1: Seismicity parameter values from ETAS inversion and those used in subsequent calculations
* The value of *α* is fixed in ETAS inversions

CHAPTER 3

-OBJECTIVE 1: LOCAL SEISMICITY RATES-

We suggested previously that seismicity rate might scale with injected volume. To test this claim, we use ETAS to track changes in background seismicity rate and compare these variations to variations in fluid productivity. We do an ETAS inversion for two-year windows of seismicity data centered on each month of production and injection for the Salton Sea geothermal field (Figure 3.1). The time window is chosen to ensure there are enough data points for a stable inversion. The resulting vector of μ values for each month is essentially a smoothed curve of background seismicity rate as a function of time. In this context, background rate means the non-aftershock component of the seismicity and can vary over time.

We find that the background rate very closely imitates any metric of fluid volume (injection, production, or net production, defined here as production minus injection) in the earlier years of injection (1982 to about 1992) when multiplied by an appropriate constant. In later years (2006 to 2011), μ is only tracked by net production (Figure 3.1). The proportionality constant for net injection increases from $8 \cdot 10^6$ to $2 \cdot 10^7$ EQs/day/m^3/month and over our observation time (1982 to 2012). This analysis contains no detailed information about well activity, but a simple plot of production and injection well activity (Figure 3.2) indicates that highest correlation occurs during the initial phase of well proliferation in the field, and later, during a period of time when most wells have been established and there is relatively little change the pattern of injection and production.

We conclude that net production volume provides the best way to estimate seismic response, and stress the significance of this result given that most studies find seismicity rates proportional to injected volume (Shapiro et al., 2010). If earthquakes are indeed responding to net volume as we assert, a possible implication is that seismicity responds to higher hydraulic gradients or stress gradients between injection and production wells within the reservoir, and not to simply to the diffusion of high pore pressures at injection sites. The shift to a higher proportionality constant in later years also suggests that geothermal fluid exploitation becomes less efficient at inducing earthquakes with time, requiring higher volumes to induce the same number of events.

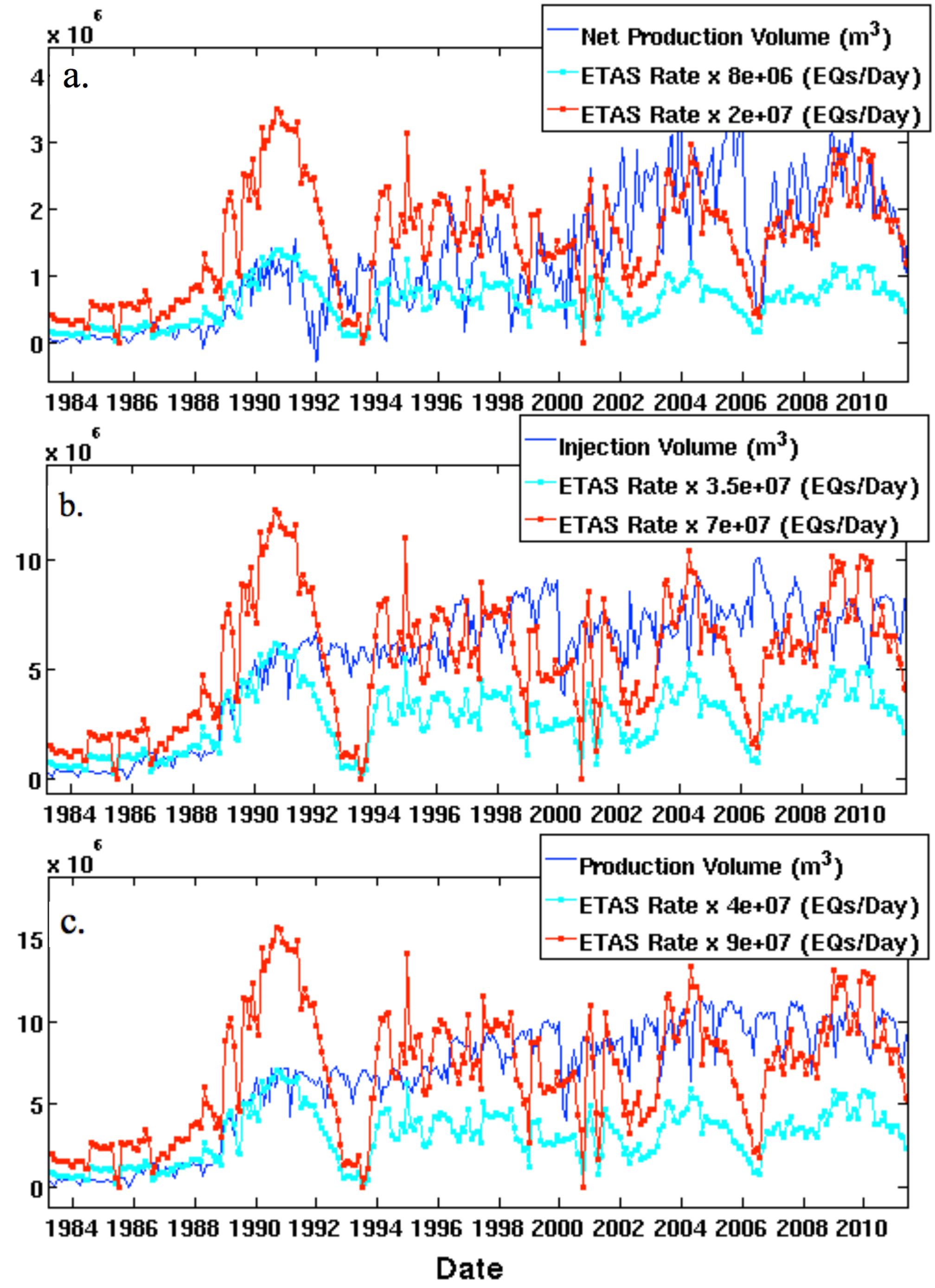

Figure 3.1: ETAS-derived background rate (μ) over time compared to fluid volumes at the SSGF. Dark blue curves represent fluid volume, cyan and red curves are background rate multiplied by constants that seek to match the fluid volume curve. Figure 3.1a: Background rate compared to net production. The background rate, μ, tracks the net fluid production over early and late periods of operation. However, the constant varies in the different operational intervals of the field. In the early part of the catalog (1982 – 1991), $\mu \approx 8 \cdot 10^6$ EQ/day/m^3 (cyan); in later years (2006-2012), $\mu \approx 2 \cdot 10^7$ EQ/day/m^3 (red). Figures 3.1b and 3.1c: Background rate compared to injection and production volumes. The background rate only tracks injected and extracted volumes for the early part of the catalog (1982-1991) and there is no constant that μ can be multiplied by to match either rate in any other appreciable section of the catalog.

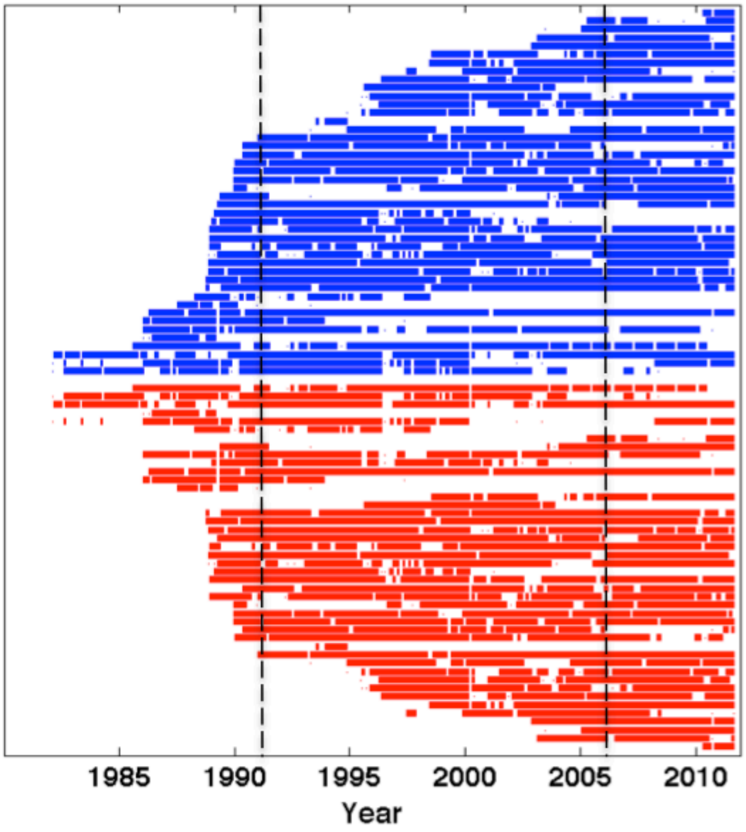

Figure 3.2: Plot of activity periods for injection (blue) and production (red) wells in the SSGF. The dashed lines approximate times where there is a change in correlation between net volume and background seismicity. There is good correlation between 1982 and ~ 1991, when there is a huge proliferation of wells, and from ~ 2006 to present, when there is little change in well activity field-wide.

CHAPTER 4

-OBJECTIVE 2: AFTERSHOCK PRODUCTIVITY-

Having established a link between net production volume and background seismicity rate, we investigate how the aftershock productivity of the triggered events compares to that of other, non-triggered earthquakes. We first calculate *K* and α for the Salton Sea geothermal field and describe corrections that must be done to *K* to remove catalog biases then compare these values to those calculated by our ETAS inversions. Finally, we calculate aftershock productivity for 9 study regions in California and determine the relative efficiency of earthquakes in the SSGF at generating aftershocks.

4.1 CALCULATING K AND α

The number of aftershocks triggered by a mainshock of magnitude, *M*, is given by

$$N_{aft} = K_R \cdot 10^{\alpha(M-M_c)} \tag{4}$$

(Reasenberg and Jones, 1989). The parameters K_R and α can be calculated by regressing a straight line through a semi-log plot of aftershock counts versus mainshock magnitude. Parameter α is the slope of the fitted line; K_R is the y intercept.

We restrict the definition of mainshock to those events within a given study area that are neither preceded nor followed by a larger event within 20 days or 100 km and aftershocks as those events that follow a mainshock within 0.5 days and 5 km, even if they lie outside of the defined area for a given study region. We use stationary time and distance windows for mainshock searching and aftershock counting (rather than scale our search criteria to the size of the mainshock) to avoid assuming values for scaling constants, and because the distance decay of aftershocks as a function of mainshock magnitude is not well understood. These isolation criteria are verified with an ETAS model such that the seismicity rate following a single, isolated mainshock at some time, t_E, and distance, R, is given by

$$R_{ETAS}(t_E, R) = \frac{K \cdot 10^{\alpha(M-M_c)}}{(t_E + c)^p \cdot R^\gamma} \tag{5}$$

Parameter γ is set to 1.4 following the work of Felzer and Brodsky (2006). In counting aftershocks, we seek to capture as many events as possible while keeping the time and distance windows restrictive enough that the number of background events counted is minimized. Therefore, time and distance windows are chosen to capture ~95% of the events following any mainshock. Integrating over all of space and time gives the total number of expected aftershocks, so we define a time T such that the temporal integral from t_{min} to T over all space is 95% of the total number of aftershocks such that

$$0.95 = \frac{\int_{t_{\min}}^{T} \int_{R_{\min}}^{R_{\max}} \frac{K \cdot 10^{\alpha(M-M_c)}}{(t_E + c)^p \cdot R^\gamma} dR dt_E}{\int_{t_{\min}}^{t_{\max}} \int_{R_{\min}}^{R_{\max}} \frac{K \cdot 10^{\alpha(M-M_c)}}{(t_E + c)^p \cdot R^\gamma} dR dt_E} \tag{6}$$

The spatial integral and the numerator terms of R_{ETAS} drop out, so the resulting integral with $t_{min} = 0$ and $c = 0.006$ gives $T = 0.5$ days. Equation 6 is undefined for $R_{min} = 0$, so the spatial aftershock counting window is defined by the distance at which the rate of aftershocks 0.5 days following a magnitude 3 mainshock (95% of events in the Salton Sea geothermal field have magnitude ≤ 3) falls to less than the background rate of seismicity, $\mu = 0.11$ EQs/day; a distance of 5 km (Figure 4.1).

Mainshock windows are similarly found from spatial and temporal decay of aftershocks following a magnitude six earthquake, which is larger than the largest event on record for the Salton Sea geothermal field (Figure 4.2). For mainshocks, we simply look for the time at which seismicity rate is ≤ 1/day at a distance of 5 km and the distance at which seismicity rate is ≤ 1/day at 0.5 days; 20 days and 100 km, respectively.

Mainshocks are binned into 0.1 magnitude unit bins such that the magnitude 3.2 bin includes mainshocks of magnitude greater than 3.15 and less than or equal to 3.25. The mean aftershock value for each bin is simply the mean of the aftershock counts for all mainshocks within a given bin. Values of K_R and α (plus error bars) are calculated using a general least squares method to fit a straight line through a plot of mainshock magnitude (bin center values) versus the logarithm of the mean number of aftershocks (Figure 4.3) (Press et al., 2007). We find that $\alpha = 1.03 \pm 0.3$ (Table 4.1) and $K_R = 0.001$ with uncertainty bounds between $5 \cdot 10^{-5}$ and $2 \cdot 10^{-2}$ for the Salton Sea geothermal field.

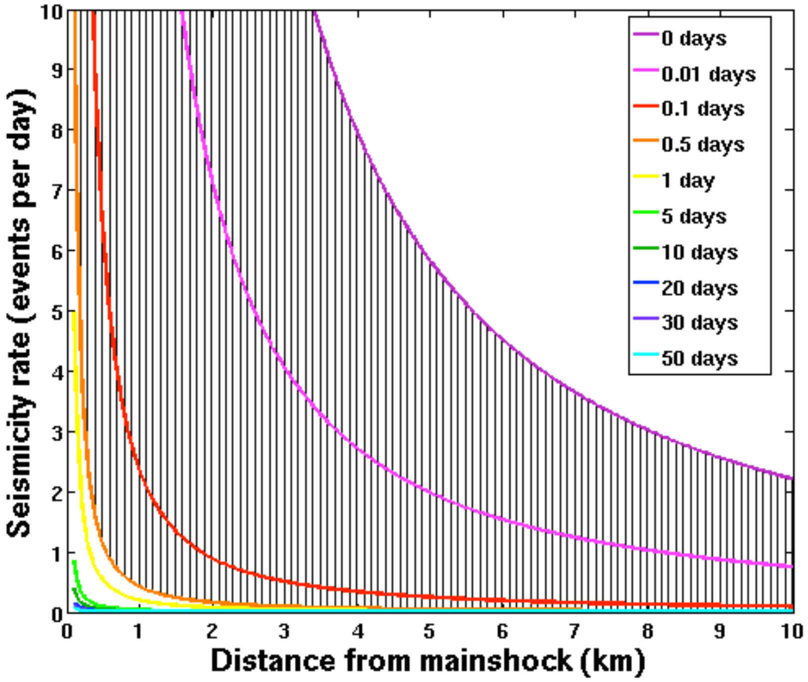

Figure 4.1: Seismicity rate as a function of distance for various times following a magnitude 3 mainshock. The integral of any curve is the total number of earthquakes that occur following that time. The shaded area shows the time interval in which 95% of aftershocks occur, 0 to 0.5 days.

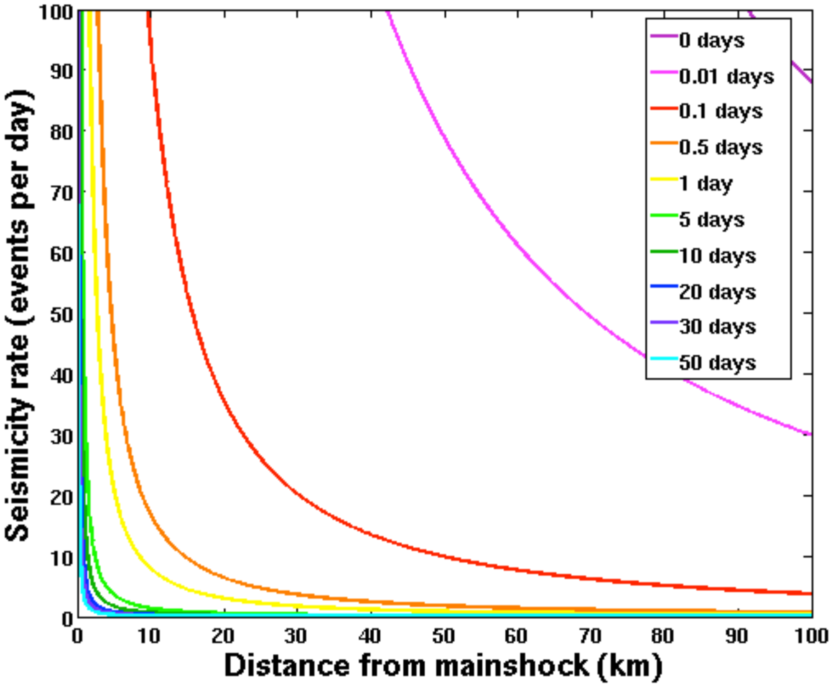

Figure 4.2: Seismicity rate as a function of distance for various times following a magnitude 6 mainshock. Seismicity rate decays to < 1/day at a distance of 5 km after 20 days, and to < 1/day at 0.5 days out at a distance of 100 km.

4.2 CORRECTING K

While the calculated value of α confirms our assumption that $\alpha \approx 1$ for our ETAS inversion of SSGF earthquakes, two corrections must be done to K_R before it can be compared to the value of K returned by our ETAS inversions (K_E), one for magnitude completeness of K_R, and the other to account for the time integral (summation) in ETAS. The magnitude correction must be done because Figure 4.3 plots

$$N_{aft} = K_R \cdot 10^{\alpha M} \tag{7}$$

without any consideration of the minimum magnitude of the catalog. The correction to K_R that must be done to properly fit equation 4 is

$$K_{R\_mag} = K_R \cdot 10^{\alpha M_c} \tag{8}$$

which for the calculated value of and M_c and our calculated value of $\alpha = 0.995$, gives $K_{R\_mag} = 6.2 \cdot 10^{-2}$. This must then be modified to match the ETAS solution for a single aftershock sequence

$$N_{aft\_E} = \int_{t_{\min}}^{t_{\min}} \frac{K_E \cdot 10^{\alpha(M-M_c)}}{(t_E + c)^p} dt_E \tag{9}$$

which, after taking the derivative with respect to t_E gives

$$N_{aft\_E} = \left(\frac{(t_{\max} + c)^{1-p}}{1-p} - \frac{(t_{\min} + c)^{1-p}}{1-p} \right) \cdot K_E \cdot 10^{\alpha(M-M_c)} \tag{10}$$

Using $p = 1.1$, $c = 0.006$, and the aftershock counting windows t_{min} and t_{max} of 0 and 0.5 days, respectively, we get

$$N_{aft\_E} = 5.96 \cdot K_E \cdot 10^{\alpha(M-M_c)} \tag{11}$$

which we can compare to equation 4 and see that

$$K_{R\_mag} = 5.96 \cdot K_E \tag{12}$$

Dividing K_{R_mag} by 5.96 gives $8.1 \cdot 10^{-3}$ with uncertainty bounded between $5 \cdot 10^{-4}$ and 0.15 (Table 4.1), which puts the calculated values of K_{R_mag} and K_E within error of each other and lends support to our assertion that our ETAS results for both K and α are robust.

Parameter	*ETAS value*		*Calculated value*	
$\boldsymbol{K}$	$1.3 \cdot 10^{-2}$	$\pm 1.4 \cdot 10^{-3}$	$*8.1 \cdot 10^{-3}$	$[5 \cdot 10^{-4}\ 0.15]$
$\boldsymbol{\alpha}$	**1	--	1.0	± 0.3
$\boldsymbol{c}$	0.30	$\pm 4.0 \cdot 10^{-2}$	$6 \cdot 10^{-3}$	--
$\boldsymbol{p}$	1.5	$\pm 5.5 \cdot 10^{-2}$	--	--
$\boldsymbol{\mu}$	0.11	$\pm 4.6 \cdot 10^{-3}$	--	--

Table 4.1: ETAS and calculated seismicity parameter values
* value of K reported is the fixed value, $K_{R\_mag}/5.96$
** α is fixed at 1.0 in the ETAS inversion, and is not calculated

4.3 REGIONAL VARIATIONS IN AFTERSHOCK PRODUCTIVITY

To test whether aftershocks are triggered at different rates inside and outside of the geothermal fields, we calculate productivity parameters K and α for each of nine non-geothermal study regions and compare them to the values calculated for geothermal fields. All study sites are located within the coverage area of the relocated Hauksson, Yang, and Shearer (2012) catalog, which covers most of southern California (Figure 4.4). We consider the Salton Sea and Coso geothermal fields, and neglect the Brawley geothermal field because it is small and lacks sufficient data for these calculations. The SSGF study area is the same as defined by Llenos et al. (2009) and the Coso geothermal study area is fitted to the size of the field. The remaining study areas are centered around the Hollister, Parkfield, Lake Isabella, Landers, Los Angeles, the San Bernadino mountains, a part of the San Jacinto fault, and the southern part of the Elsinore fault. Non-geothermal study areas are 0.5 degrees across in both latitude and longitude. We also calculate productivity parameters for all events in southern California. Study area sizing attempts to minimize internal tectonic variability while still encompassing enough data points to make meaningful calculations.

Results show that the geothermal areas studied, Coso and SSGF, have more aftershocks per mainshock, on average, than the other study areas within southern California (Figure 4.3). The study areas located on the creeping section of the San Andreas Fault (Hollister and Parkfield), have a correspondingly lower aftershock productivity, as expected for an area that nucleates relatively few earthquakes.

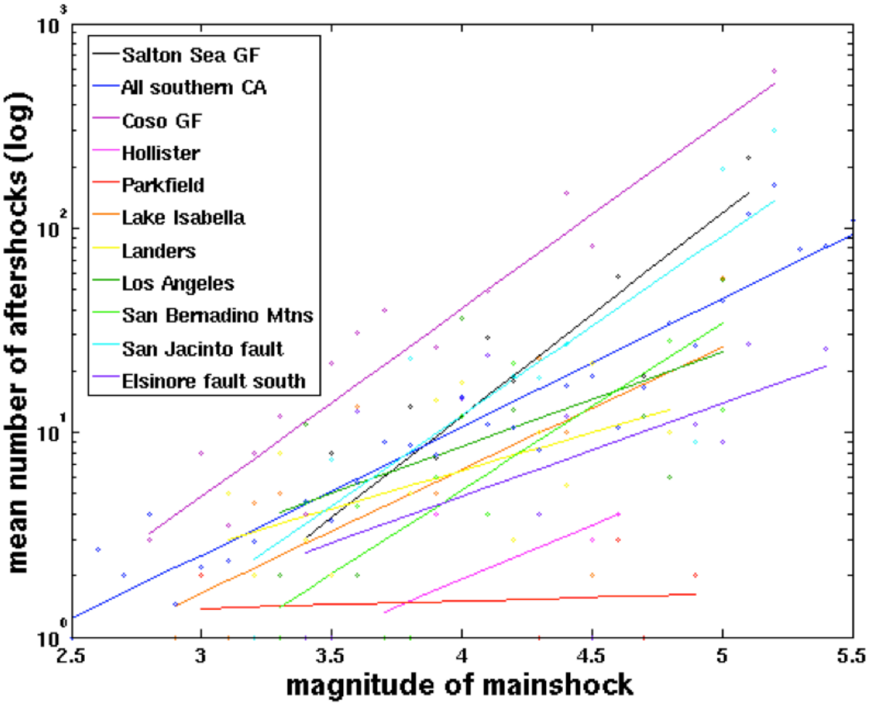

Figure 4.3: Linear regression of mean aftershock productivity. The Coso and Salton Sea geothermal fields have higher aftershock productivity than most other study areas in CA. Hollister and Parkfield, located on the creeping section of the SAF, have very low aftershock productivity.

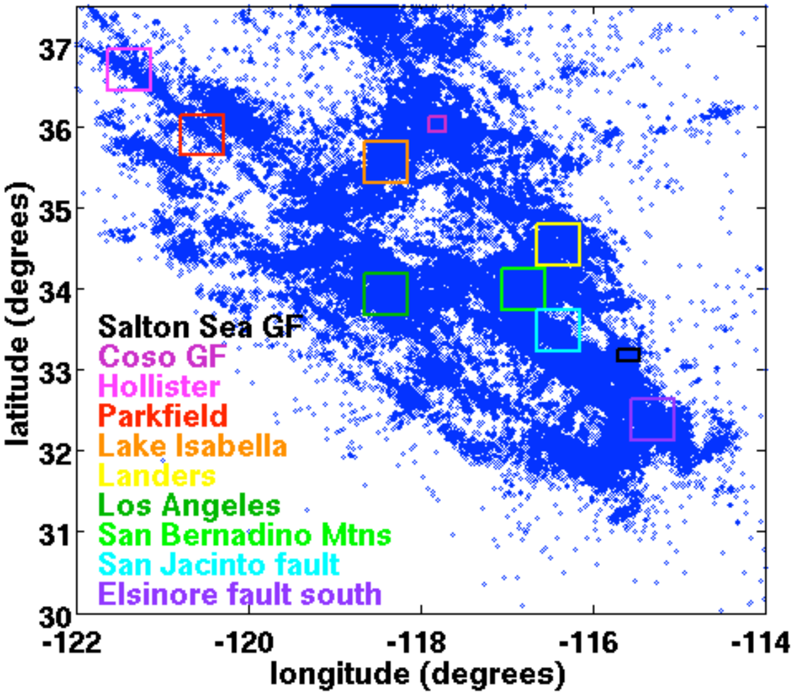

Figure 4.4: Location of study areas used in aftershock productivity calculations. Blue dots are earthquake epicenters of earthquakes in the HYS relocated catalog (Hauksson et al., 2012)

CHAPTER 5

-OBJECTIVE 3: THE SAN ANDREAS QUESTION-

To assess the hazard that geothermal energy generation presents to society, we examine the probability that the aftershocks of induced earthquakes within the geothermal fields might trigger societally significant events. The goal of this section is to provide a framework for how to think about induced seismicity and remote triggering, and so we build up in stages, beginning with calculating the probability of a single event triggering another local event, and ultimately, the probability of a catalog of events triggering an event anywhere along a regional fault.

5.1 POISSONIAN PROBABLITY

As usual, we assume that seismicity is a Poissonian process whose rate is described by an ETAS model, and further assume that this relationship holds for induced seismicity in geothermal fields (Langenbruch et al., 2011). For a homogeneous Poissonian process, the probability of having *k* events in some time window, t_p, is

$$P(k) = \frac{e^{-\lambda \cdot tp} \cdot (\lambda \cdot tp)^k}{k!} \tag{13}$$

where λ is the Poissonian rate (Blom, 1989). The probability of having more than *k* events in that time window is then

$$P(>k) = 1 - \sum_{i=0}^{k} P(i) \tag{14}$$

So to find the probability of triggering any number of earthquakes in the field, we substitute a modified ETAS rate model (R_{ETAS}) into λ and calculate the probability of triggering greater than zero events, or P(>0). Our probability becomes

$$P(>0) = 1 - e^{-R_{ETAS} \cdot t_P} \tag{15}$$

and we use this formula for all following probability calculations, together with parameter values listed in Table 5.1.

ETAS parameter	*Assigned Value*
K	$1.3 \cdot 10^{-2}$
α	1.1
c	0.006
p	1.1
μ	0.11
γ	1.4
b	1.02
M_c	1.7

Table 5.1: List of parameter values used in probability calculations for Chapter 5

5.2 TRIGGERING A LOCAL EVENT WITH A SINGLE MAINSHOCK

For the Salton Sea geothermal field, specifically, we do a preliminary calculation of the probability that a single earthquake within the field will trigger a larger event anywhere in the field. We use SSGF exclusively in early examples because ETAS parameters cannot be calculated for Brawley and are later assumed to be equal to those for the SSGF. We arbitrarily choose magnitudes five and seven for the triggerer and the triggered event, respectively.

The ETAS model we use for the seismicity rate at some time, t_E, (subscript given to differentiate it from the time used in Poissonian probability) after a triggering event for this calculation takes the form

$$\mathrm{R}_{ETAS\_\mathrm{mod}}(t_E) = \frac{K \cdot 10^{\alpha(M-M_c)}}{(t_E + c)^p} \tag{16}$$

because we only consider a single mainshock, and can neglect μ and simplify ETAS to only account for the aftershocks of a single event. The productivity constant K is referenced to the magnitude of completeness (M_c) of events the catalog it is calculated from, such that $\mathrm{R}_{\mathrm{ETAS}}$ is the rate of earthquakes $\geq M_c$. To find $\mathrm{R}_{\mathrm{ETAS}} \geq$ the magnitude of the triggered event (M_{ref}), K needs to be adapted to the size of earthquake we trigger, so we define a modified K such that

$$K_{mag} = K \cdot 10^{-b(M_{ref}-M_c)} \tag{17}$$

where b is the Gutenberg Richter exponent for the Salton Sea geothermal field (Appendix C). As will be discussed in more detail to follow, K is also dependent on the temporal and spatial extent of the catalog used to generate it. In this simple formulation, no further adjustments to K need to be done if we consider the situation where the earthquake rate is constant over a time t_P that is equal to the time scales used in observing K, in this case the maximum time after a mainshock that aftershocks were counted, or 0.5 days.

The full probability of triggering a magnitude seven due to a magnitude 5 at the Brawley geothermal field becomes

$$P_{trig}(>0) = 1 - e^{-\frac{K_{mag} \cdot 10^{-b(M_{ref}-M_c)} \cdot 10^{\alpha(M-M_c)}}{(t_E+c)^p} \cdot t_p} \tag{18}$$

and in this initial example, we use our best estimates of K, c, α, p, b, and M_c from the Salton Sea geothermal field (Table 5.1). The Omori decay time constant, t_E, is arbitrarily set to one day, or one unit length of time, $M = 5$, and $M_{ref} = 7$. The value of *b* is calculated using the maximum likelihood formulation of Aki (1965) and is equal to 1.02 for all events greater than magnitude 1.7 in the SSGF.

The resulting probability of a magnitude seven earthquake given a magnitude five becomes $P_{trig}(>0) = 5.1 \cdot 10^{-5}$, when all of the appropriate parameter values are substituted in. This probability represents the chance that an earthquake of magnitude seven will be triggered anywhere in the Salton Sea geothermal field in any given 0.5 day window following a local magnitude five earthquake. If we reduce the magnitude of the triggering event to magnitude four, the probability that any given magnitude four event will trigger a magnitude seven event within 0.5 days goes down to $5.1 \cdot 10^{-6}$. The catalog of Salton Sea geothermal events contains only 14 events with magnitudes greater than four, and there has never been a magnitude seven, so this very simple probability is not obviously contradicted.

5.3 REMOTE TRIGGERING AT A POINT WITH A SINGLE MAINSHOCK

The next degree of complexity added is distance decay, and we pose the question: what are the chances of the same magnitude five pre-cursor triggering a magnitude seven event on the proximal San Andreas fault? We must now account for distance in our probability calculations, and so modify our seismicity rate to reflect the distance decay of aftershocks by adding distance decay parameter, γ. Recall from equation 5 that seismicity rate at time t_E after an earthquake follows

$$\mathrm{R}_{ETAS}(t_E, R) = \frac{K \cdot 10^{\alpha(M-M_c)}}{(t_E + c)^p \cdot R^\gamma}$$

such that the seismicity rate at distance *R* from the location of the mainshock (whether it be on a fault or otherwise) is simply the rate of aftershocks decayed as $R^{-\gamma}$

to the triggering location of interest. For the mainshock location and triggering location, we choose the center of the geothermal field and the southern end of the San Andreas fault near Bombay Beach as mapped by the USGS, respectively.

This new formulation of ETAS is a function of both distance and time, and so both spatial and temporal corrections to parameter K are necessary to ensure that it properly represents the aftershock productivity and is not biased by aftershock counting windows which include most, but not all, aftershocks. We first do a time correction, defining a new parameter, K_{time}, that represents the value of K with temporal windowing biases removed. K_{time} is found by setting the number of aftershocks expected from the aftershock productivity equation (equation 4) equal to the time integral of the time-dependent (without spatial terms) form of R_{ETAS}, where

$$K \cdot 10^{\alpha(M-M_c)} = \int_{t_{\min}}^{t_{\max}} \frac{K_{time} \cdot 10^{\alpha(M-M_c)}}{(t_E + c)^p} dt_E \tag{19}$$

is solved for K_{time}. The integration yields

$$K_{time} = \frac{K \cdot (1-p)}{(t_E + c)^{1-p} \Big|_{t_{\min}}^{t_{\max}}} \tag{20}$$

evaluated according to the limits of integration defined by the aftershock counting windows, 0 to 0.5 days. The temporal correction for K take this form (and not a logarithmic one), because we assume, as before, that $p = 1.1$.

The distance correction could be done the same way, except that the integral of $R^{-\gamma}$ is undefined for $R = 0$ (there is no distance equivalent to c in our equations). Instead, we simply relax our distance window for aftershocks and count the fraction, χ, of aftershocks that lie at a distance greater than 5 km from the mainshock in the Salton Sea geothermal field. We find that $\chi = 4\%$, so $(1- \chi)$, or 96% represents the fraction of the distance integral of counted events to the distance integral of total events and

$$(1-\chi)\cdot K_{time\&dist} = K_{time} \tag{21}$$

Applying the magnitude correction results in

$$K_{time,dist\&mag} = \frac{K\cdot 10^{-b(M_{ref}-M_c)}\cdot(1-p)}{(1-\chi)\cdot(t_E+c)^{1-p}\Big|_{t_{\min}}^{t_{\max}}} \tag{22}$$

and the non-background seismicity rate becomes

$$\mathrm{R}_{ETAS}(t_E,R) = \frac{K_{time,dist\&mag}\cdot 10^{\alpha(M-M_c)}}{(t_E+c)^p\cdot R^{\gamma}} \tag{23}$$

This new formulation of $K_{time,dist\&mag}$ eliminates temporal and spatial effects on K and adjusts the seismicity rate to a higher reference magnitude. Biases in catalog selection and completeness have been removed, and time and spatial windows (t_E and R) over which rates and probabilities are estimated no longer need to relate to the specific catalog or methods by which K is calculated. We decide, therefore, that it is intuitively simple to consider the probability that a magnitude seven earthquake occurs at the southern end of the San Andreas Fault within a year of a magnitude five event in the SSGF.

Omori's law dictates that seismicity decays in time following a mainshock as t^{-p} (Omori, 1894; Utsu, 1961), so we cannot assume that seismicity rate is constant in the year following a magnitude 7 event. We assume, however, that seismicity rate is constant over much smaller time windows and calculate seismicity rate and resulting probability for each day following a mainshock, such that t_E is a vector of [1:365] and t_p is the interval over which we are assuming seismicity rate is constant, one day. The summation of these probabilities gives an approximation to the probability of a magnitude five event triggering a magnitude seven or larger earthquake on the San Andreas fault within a year.

Plugging R_{ETAS} into Equation 15 gives a probability of $4.7 \cdot 10^{-5}$ (Table 5.2). For a magnitude four triggerer, the probability falls to $4.7 \cdot 10^{-6}$ per magnitude four event per year. With only 14 magnitude four earthquakes in the Salton Sea geothermal field since 1980 and no magnitude sevens on the San Andreas fault since then, these calculations are plausible.

The probabilities for the Brawley geothermal field are calculated with the triggering distance, *R*, being the separation between the center of the BGF and the northern end of the Imperial fault as mapped by the USGS (Table 5.2). We assume that the values of the remaining parameters are the same as calculated for the Salton Sea geothermal field because the Brawley dataset is too small to reliably compute these parameters and the fields are tectonically and geologically similar.

Triggered event magnitude	*Triggered event location*	*Trigger*	*Trigger location*	*Probability time **	*Probability*
5	Bombay	One M5	SSGF	1 year	$5.1 \cdot 10^{-3}$
5	North IF	One M5	BGF	1 year	$3.6 \cdot 10^{-3}$
5	Bombay	One M5	SSGF	1 day	$1.0 \cdot 10^{-3}$
5	North IF	One M5	BGF	1 day	$7.1 \cdot 10^{-4}$
7	Bombay	One M4	SSGF	1 year	$4.7 \cdot 10^{-6}$
7	North IF	One M4	BGF	1 year	$3.3 \cdot 10^{-6}$
7	Bombay	One M5	SSGF	1 year	$4.7 \cdot 10^{-5}$
7	North IF	One M5	BGF	1 year	$3.3 \cdot 10^{-5}$

Table 5.2: Remote triggering probabilities for nearest point on a fault from a single mainshock
*Probability time = time following mainshock over which probability is calculated.

5.4 REMOTE TRIGGERING ON A FAULT WITH A SINGLE MAINSHOCK

The final consideration that must be taken into effect for a single mainshock is that an earthquake can nucleate anywhere along the length of a fault, and so we must integrate R_{ETAS} along the entire length to get the probability of triggering the full fault. Integrating over each infinitesimally small section of fault, *dR*, from the closest and farthest distances on the fault to the mainshock (R_{min} and R_{max}) gives

$$\mathrm{R}_{ETAS}(t_E,R)=\frac{K_{time,dist\&mag}\cdot 10^{\alpha(M-M_c)}}{(t_E+c)^p\cdot(1-\gamma)}\cdot(R_{\max}^{1-\gamma}-R_{\min}^{1-\gamma}) \tag{24}$$

We again calculate R_{ETAS} for each day following a mainshock and report the annual probability as the sum of the contributions from each day in that time span (Table 5.3).

Triggered event magnitude	*Trigger location*	*Triggered fault*	*Probability*
5	SSGF	SAF	$7.2\cdot10^{-4}$
5	BGF	IF	$7.0\cdot10^{-4}$
7	SSGF	SAF	$6.5\cdot10^{-6}$
7	BGF	IF	$6.4\cdot10^{-6}$

Table 5.3: Remote triggering probabilities for entire fault from a single, M5 mainshock

5.5 REMOTE TRIGGERING ON A FAULT WITH AN EARTHQUAKE CATALOG

For a catalog of events, R_{ETAS} includes contributions from both background rate and aftershock rate. Background events by definition lie inside of the field and so for distant triggering probabilities we continue to only consider aftershock rate ($\lambda_{aftershocks}$). $\lambda_{aftershocks}$ is simply a more complicated formulation of equation 24 and is given by

$$\lambda_{aftershocks}(t_E,R)=\sum_{i=1}^{N}\frac{K_{time,dist\&mag}\cdot 10^{\alpha(M_i-M_c)}}{(t_E-t_i+c)^p\cdot(1-\gamma)}\cdot R_i^{1-\gamma}\Big|_{R_{i\_\min}}^{R_{i\_\max}} \tag{25}$$

such that the aftershock rate of at some time, t_E, is dependent on the history of all events that precede it. Here, the subscript i denotes the index of all earthquakes that occur prior to t_E, where M_i, and t_i are the respective magnitude and time of the i^{th} event in the catalog. For the example of induced seismicity in the Salton Sea geothermal field triggering an earthquake on the San Andreas fault (SAF), R_i is the distance from each earthquake in the field to the near and far triggering points (R_{i_min} and R_{i_max}) at either end of the SAF (Bombay Beach and the southern end of the creeping section). Similarly, for Brawley R_i is computed between each earthquake and the northern and southern ends of the Imperial fault (IF).

$\lambda_{aftershocks}$ is again calculated for each day. Here, t_P is set to one day, t_E becomes the day (date) of interest, and the daily probability is calculated for each day using $\lambda_{aftershocks}$ for the Poissonian rate following

$$P_{aftershocks}(>0)=1-e^{-\lambda_{aftershocks}\cdot t_p} \tag{26}$$

The annual probability is simply the sum of daily probabilities for a given year.

We calculate the probability of triggering a magnitude seven or larger event for both scenarios (SSGF triggering the SAF and BGF triggering the Imperial fault) for the years 1981 to 2011 (Figure 5.1). In 2005, the most seismically active year on record for the SSGF, the calculated probability of triggering a magnitude seven event on the SAF is $1.7\cdot10^{-4}$; the corresponding probability for the BGF and Imperial fault in 2005 is $2.6\cdot10^{-7}$ (Table 5.4). The highest probability for BGF and IF, $7.0\cdot10^{-6}$, occurs in the year with the highest moment release (2010) and not the highest number of earthquakes, highlighting the triggering power of larger earthquakes relative to smaller ones. The probability for the SSGF and SAF in 2010 is $4.5 \cdot 10^{-6}$. For most years, the probability for the SSGF/SAF lies between 10^{-5} and 10^{-6}; the probability for the BGF/IF is more variable but is generally bounded between 10^{-6} and 10^{-8} (Figure 5.1).

Triggered event magnitude	***Catalog***	***Year***	***Fault Triggered***	***Probability from aftershocks***
5	SSGF	2005	SAF	$1.3 \cdot 10^{-2}$
5	BGF	2005	IF	$2.8 \cdot 10^{-5}$
7	SSGF	2005	SAF	$1.7 \cdot 10^{-4}$
7	BGF	2005	IF	$2.6 \cdot 10^{-7}$
5	SSGF	2010	SAF	$4.9 \cdot 10^{-4}$
5	BGF	2010	IF	$7.7 \cdot 10^{-4}$
7	SSGF	2010	SAF	$4.5 \cdot 10^{-6}$
7	BGF	2010	IF	$7.0 \cdot 10^{-6}$

Table 5.4: Probabilities for 2005 and 2010 earthquakes in the SSGF and BGF triggering the San Andreas Fault (SAF) or Imperial Fault (IF). For these years, we also compute the probabilities for triggering magnitude 5 events on each fault.

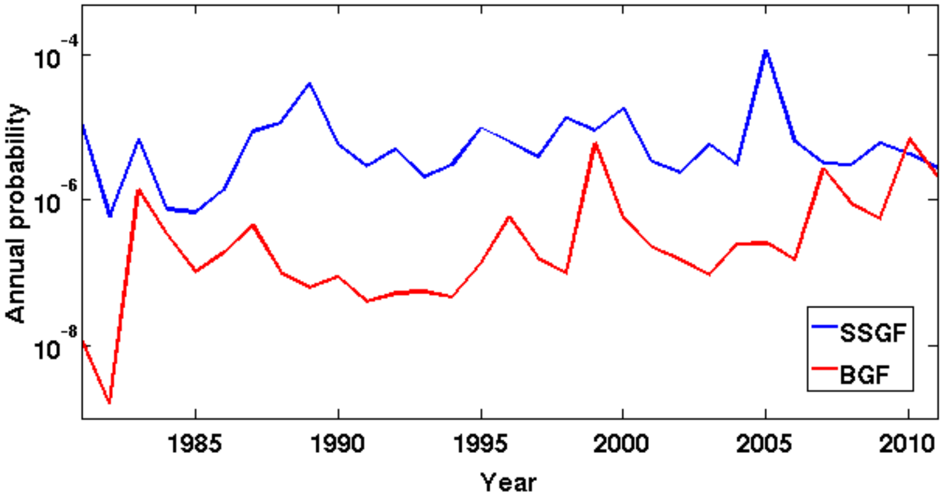

Figure 5.1: Annual probabilities of the SSGF triggering the SAF and the BGF triggering the IF. Highest probabilities occur in 2005 for the SSGF/SAF and 2010 for the BGF/IF.

CHAPTER 6

-CONCLUSIONS-

6.1 SUMMARY AND CONCULSIONS

In determining the seismic hazard that the Salton Sea and Brawley geothermal fields pose in southern California, we examine whether or not fluid injection has a significant effect on seismicity rate, determine the aftershock productivity of the SSGF compared with other regions in California, and calculate the probability that each geothermal field will trigger a societally significant event on a large, proximal fault.

For the Salton Sea geothermal field, we find significant evidence from spatial and temporal plots of seismicity to suggest that seismicity is being induced by fluid injection. This is substantiated by the ETAS-derived background rate varying temporally in concert with monthly net extracted volume during the periods of ~1982 to 1991 and ~2006 to present. The constant of proportionality between background seismicity rate and monthly net production volume increases from $8 \cdot 10^6$ EQs/day/m^3/month in the early period to $2 \cdot 10^7$ EQs/day/m^3/month, suggesting that fluid injection and extraction becomes less efficient at triggering earthquakes with time. We find, in examining aftershock productivity, that the induced earthquakes at the SSGF are more effective at generating aftershocks than other earthquakes in non-geothermal areas of southern California. A higher rate of aftershocks also provides more opportunity for remote triggering of regional faults. Despite high aftershock productivity, the highest calculated annual probability of triggering a magnitude seven earthquake on the San Andreas fault (only 24 km distant) between 1981 and 2011 is only $4.9 \cdot 10^{-4}$.

Less data (for both seismicity and fluid extraction and injection) is available for the Brawley geothermal field, but qualitative observations indicate a strong probability that high injection, production, and/or net production volumes elicit a strong seismic response. There is also insufficient seismic data to measure aftershock productivity but we suggest that earthquakes in the Brawley geothermal field might also generate more aftershocks than other events, citing tectonic similarities between the locations of the BGF and SSGF and evidence that geothermal areas may have higher aftershock productivity than other areas. The highest calculated probability in our observation time for the BGF triggering a magnitude seven or larger the Imperial fault is $7.0 \cdot 10^{-6}$ in 2005.

Addressing our motivating questions, we conclude that injection and production, and net production volume in particular, at both the Salton Sea and Brawley geothermal fields locally increase seismicity rate. Additionally, we establish that the SSGF has higher aftershock productivity than other areas in southern California, and assert that the same may be true of the BGF and other geothermal areas. Finally, we determine that the aftershocks of events within each geothermal field has a small, but finite, chance of triggering a large magnitude earthquake on proximal large faults.

6.2 FUTURE WORK

In the future, we would like to combine our results with earthquake hazard models to account for the fact that some faults are more likely to rupture than others, without the added effect of proximal geothermal activity and induced seismicity. The 2007 Working Group on California Earthquake Probabilities, for example, calculated a 59% likelihood of the southern San Andreas fault will rupture to produce a magnitude 6.7 or larger event in the next 30 years (Field et al., 2008). Because the San Andreas fault is already near failure, the probabilities we calculated are likely lower bounds.

We would also like to calculate triggering probabilities directly from fluid volumes. We contend, in the case of the SSGF, that background seismicity rate is the product of net production volume multiplied by a constant ($2{\cdot}10^7$ in the years from ~2006 to present), so if we could calculate the branching ratio (proportion of aftershocks to mainshocks in an area) for the Salton Sea geothermal field, we could estimate the rate of aftershocks as the product of the branching ratio, monthly production volume, and our empirical constant. This rate can be used in probability calculations the same way as R_{ETAS} and $\lambda_{aftershocks}$ to find the probability of triggering a regional fault per unit volume of net produced fluid at the SSGF.

Finally, we need to confirm that there is not a change in either spatial or temporal aftershock decay parameters (p and γ) beyond the edge of the geothermal fields that would change the rate of aftershocks at distance.

APPENDICES

APPENDIX A: CALCULATING M_C FOR THE SSGF

The magnitude completeness threshold (M_C) for a seismic catalog is the magnitude above which all earthquakes are reliably detected. On a Gutenberg-Richter plot, M_C is the lower magnitude at which the data deviate from linearity (Figure A.1). To calculate M_C, we fit a straight line to the linear section of a GR plot, compute the residual between the linear fit and the data, and take the variance of data used in the linear fit. We define M_C as the point where the residual of the GR plot and linear fit becomes greater than the variance of data used in the linear fit. For the SSGF, $M_C = 1.7$.

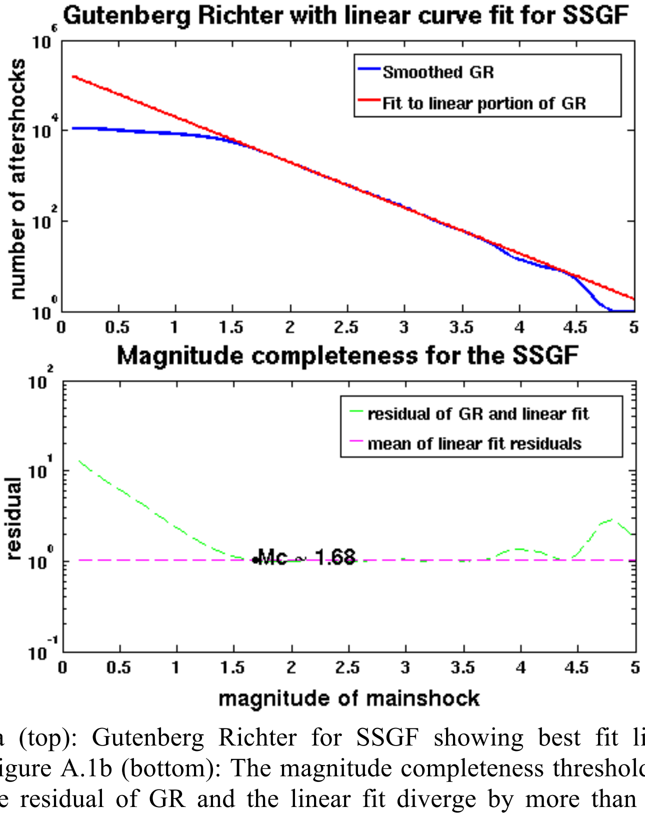

Figure A.1a (top): Gutenberg Richter for SSGF showing best fit line to linear segment. Figure A.1b (bottom): The magnitude completeness threshold is the point at which the residual of GR and the linear fit diverge by more than the standard deviation in the data points of the linear segment of GR, here $M_c = 1.7$.

APPENDIX B: CALCULATING *C* FOR THE SSGF

The parameter *c* is the average time that elapses after a mainshock before all earthquakes above *Mc* are detected. We calculate *c* by finding the amount of time required for the magnitude completeness of discrete time bins following every earthquake in our catalog to decay to the completeness threshold of the catalog as a whole (Figure 2.2). For each earthquake, we bin all subsequent events into 0.2 log unit time bins and take the magnitude completeness of each bin and after this has been done for all earthquakes in the catalog. Magnitude completeness decays exponentially, and our best-fit curve to the data falls to *Mc* of the catalog at a value of 0.006 days (Figure A.2).

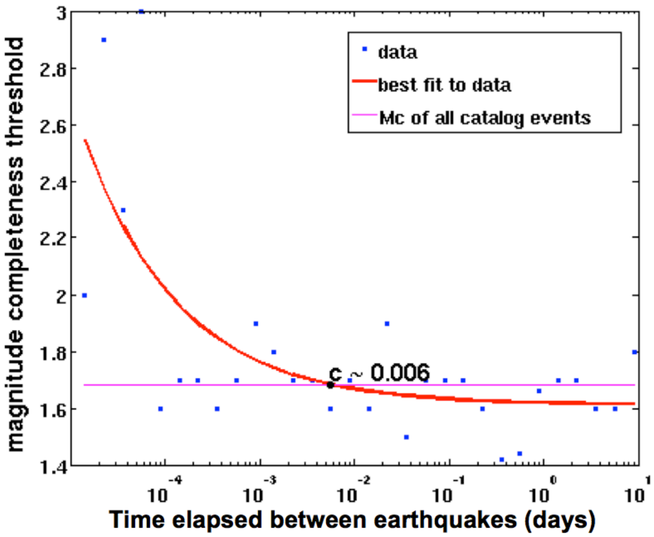

Figure A.2: Parameter *c* is calculated from the best-fit temporal decay of M_c. Earthquakes are binned into small time windows following each earthquake, the M_c of each bin is calculated, and a best-fit line is regressed through the data. The point at which the best-fit line becomes less-than M_c of the whole catalog is the best estimate for *c*.

APPENDIX C: CALCULATING THE b –VALUE FOR THE SSGF

The value of b in the Gutenberg-Richter relation

$$\log_{10} N(\geq M) = a - bM$$

is calculated using the central limit theorem presented by Aki (1965) where

$$b = \left(\frac{1}{\sum M_i / N - M_C} \right) \cdot \log_{10}(e)$$

and N is the total number of events in an earthquake catalog with magnitudes given by M_i. We find that for all events greater than or equal to magnitude 1.7 in the SSGF $b = 1.02$, which is within the typical range of 0.8 to 1.2 (Frohlich and Davis, 1993).

REFERENCES CITED

AKI, K. (1965). Maximum likelihood estimate of b in the formula log $n = a - bM$ and its confidence limits. *Bulletin of Earthquake Research Institute*, **43**: 237-239.

BLOM, G. (1989). *Probability and Statistics: Theory and Applications*. New York: Springer-Verlag.

BROOK, C. A., R. H. MARINER, D. R. MABEY, J. R. SWANSON, M. GUFFANTI, L. J. P. MUFFLER (1978). Hydrothermal convection systems with reservoir temperatures ≥ 90ºC. In *Assessment of Geothermal Resources of the United States – 1978, US Geological Survey Circular*, **790**; 18-85.

CALENERGY (2011). Worldwide Projects: Imperial Valley (United States). *CalEnergy.com* [Online]. 02 Mar. 2011. <http://www.calenergy.com/projects2d.aspx>

CALIFORNIA DEPARTMENT OF CONSERVATION (2012). GeoSteam - Query Geothermal Well Records, Production and Injection Data. *CA.gov* [Online]. 5 Dec. 2012. <http://geosteam.conservation.ca.gov/WellSearch/GeoWellSearch.aspx>

CALIFORNIA ENERGY COMMISSION (2010). Geothermal Energy in California. *CA.gov* [Online]. 02 Mar. 2011. <http://www.energy.ca.gov/geothermal/>

CHU, R. & D. V. HELMBERGER (2012). Source parameters of the shallow 2012 Brawley earthquake, Imperial Valley. *Bulletin of the Seismological Society of America*, in press.

DIPIPPO, R. (2012). *Geothermal Power Plants: Principles, Applications, Case Studies, and Environmental Impact*, *3rd ed*. Oxford: Butterworth-Heinemann.

ELDERS, W. A., R. W. REX, T. MEIDAV, P. T. ROBINSON, & S. BIEHLER (1972). Crustal spreading in southern California. *Science*, **178**: 15-24.

FELZER, K. R., R. E. ABERCROMBIE, & G. EKSTRÖM (2004). A Common Origin for Aftershocks, Foreshocks, and Multiplets. *Bulletin of the Seismological Society of America*, **94**: 88-99.

FELZER, K. R. & E. E. BRODSKY (2006). Decay of aftershock density with distance indicates triggering by dynamic stress. *Nature*, **441**: 735-738.

FIELD, E. H., T. E. DAWSON, K. R. FELZER, A. D. FRANKEL, V. GUPTA, T. H. JORDAN, T. PARSONS, M. D. PETERSEN, R. S. STEIN, R. J. WELDON II, & C. J. WILLS (2007 Working Group on California Earthquake Probabilities) (2008). The Uniform California Earthquake Rupture Forecast, Version 2 (UCERF 2). *U.S. Geological Survey Open-File Report*, **2007-1437** and *California Geological Survey Special Report*, **203**.

FROHLICH, C. & S. D. DAVIS (1993). Teleseismic b-values; or, much ado about 1.0. *Journal of Geophysical Research*, **98**: 631-644.

FUIS, G. S., W. D. MOONEY, J. H. HEALY, G. A. MCMECHAN, & W. J. LUTTER (1984). A seismic refraction survey of the Imperial Valley region, California. *Journal of Geophysical Research*, **89**: 1165–1189.

GUTENBERG, B. & C. F. RICHTER (1954). *Seismicity of the Earth and Associated Phenomena, 2nd ed*. Princeton, NJ: Princeton University Press.

HARDEBECK, J. L., K. R. FELZER, & A. J. MICHAEL (2008). Improved test results reveal that the accelerating moment release hypothesis is statistically insignificant. *Journal of Geophysical Research*, **113**.

HAUKSSON, E., W. YANG, & P. M. SHEARER (2012). Waveform Relocated Earthquake Catalog for Southern California (1981 to June 2011). Submitted to: *Bulletin of the Seismolical Society of America*, January 2012.

HELMSTETTER, A., Y. KAGAN, & D. JACKSON (2005). Importance of small earthquakes for stress transfers and earthquake triggering. *Journal of Geophysical Research*, **110**, B05S08.

LANGENBRUCH, C., C. DINSKE, & S. A. SHAPIRO (2011). Inter event times of fluid induced earthquakes suggest their Poisson nature. *Geophysical Research Letters*, **38**: L21302.

LLENOS, A. L., J. J. MCGUIRE, & Y. OGATA (2009). Modeling seismic swarms triggered by aseismic transients. *Earth and Planetary Science Letters*, **281**: 59-69.

LOHMAN, R. B. & J. J. MCGUIRE (2007). Earthquake swarms driven by aseismic creep in the Salton Trough, California. *Journal of Geophysical Research*, **112**.

MCGARR, A., D. SIMPSON, & L. SEEBER (2002). Case Histories of Induced and Triggered Seismicity. In *International Handbook of Earthquake & Engineering Seismology*. Burlington, MA: Academic Press.

MUFFLER, L. J. P., & D. E. WHITE (1969). Active metamorphism of upper Cenozoic sediments in Salton Sea geothermal field and Salton Trough southeastern California. *Geological Society of America Bulletin*, **80**: 157-182.

OGATA, Y. (1988). Statistical models for earthquake occurrences and residual analysis for point processes. *Journal of the American Statistical Association*, **83**: No. 40, 9-27.

OGATA, Y. (1992). Detection of precursory relative quiescence before great earthquakes through a statistical model. *Journal of Geophysical Research*, **97**: 19845-19871.

OMORI, F. (1894). On the aftershocks of earthquakes. *Journal of the College of Science, Imperial University of Tokyo,* **7**: 111–200.

PHILLIPS, W. S., J. T. RUTLEDGE, L. S. HOUSE, & M. C. FEHLER (2002). Induced microearthquake patterns in hydrocarbon and geothermal reservoirs: Six case studies. *Pure and Applied Geophysics*, **159** (1-3): 345-369.

PRESS, W. H., S. A. TEUKOLSKY, W. T VETTERLING, & B. P. FLANNERY (2007). *Numerical Recipes*. Third Edition. Cambridge: Cambridge University Press.

REASENBERG, P. A., & L. M. JONES (1989). Earthquake Hazard After a Mainshock in California. *Science,* **243**: 1173-1176.

REDLANDS INSTITUTE, University of Redlands (2002). *Salton Sea Atlas*. Redlands, CA: ESRI Press.

ROBINSON, P. T., W. A. ELDERS, & L. J. P. MUFFLER (1976). Quaternary volcanism in the Salton Sea geothermal field, Imperial Valley, California. *GSA Bulletin*, **87**: 347-360.

SEGALL, P. & S. D. FITZGERALD (1998). A note on induced stress changes in hydrocarbon and geothermal reservoirs. *Tectonophysics*, **289**: 117–128.

SHAPIRO, S., C. DINSKE, C. LANGENBRUCH, & F. WENZEL (2010). Seismogenic index and magnitude probability of earthquakes induced during reservoir fluid stimulations. *The Leading Edge*, **29**: 304.

SNYDER, D. L. & M. I. MILLER (1991). *Random Point Processes in Time and Space.* New York, NY: Springer-Verlag.

SOUTHERN CALIFORNIA EARTHQUAKE DATA CENTER (2012). SCSN Catalog Search (1932-Present). *California Institute of Technology* [Online]. 10 Dec. 2012. <http://www.data.scec.org/eq-catalogs/date_mag_loc.php>

TEWHEY, J. D. (1977). Geologic characteristics of a portion of the Salton Sea geothermal field. *Lawrence Livermore Laboratory,* UCRL-**52267**.

TOMPSON, A., Z. DEMIR, J. MORAN, D. MASON , J. WAGONER, S. KOLLET, K. MANSOOR, & P. MCKEREGHAN (2008). Groundwater availability within the Salton Sea basin: final report. *Lawrence Livermore National Laboratory*, TR-**400426**.

UTSU, T. (1961). A statistical study of the occurrence of aftershocks. *Geophysical Magazine,* **30**: 521-605.

UTSU, T., Y. OGATA & R. S. MATSU'URA (1995). The centenary of the Omori formula for a decay law of aftershock activity. *Journal of Physics of the Earth,* **43**: 1-33.

VAN DE KAMP, P. C. (1973). Holocene continental sedimentation in the Salton Basin, California: a reconnaissance. *Geological Society of America Bulletin*, **84**: 827-848.

YOUNKER, L.W., P. W. KASAMEYER, & J. D. TEWHEY (1982). Geological, geophysical, and thermal characteristics of the Salton Sea Geothermal Field, California. *Journal of Volcanology and Geothermal Research*, **12**: 221-258